Catalysis Science & Technology

ROYAL SOCIETY OF CHEMISTRY

PAPER

View Article Online
View Journal

Cite this: DOI: 10.1039/d5cy01610j

Engineering and optimising barium cerate-supported cobalt catalyst for ammonia synthesis

Hubert Ronduda, *[a] Małgorzata Lemańska,[a] Urszula Ulkowska,[a] Wojciech Patkowski,[a] Weronika Bulejak,[a] Andrzej Ostrowski,[a] Jacek Sikorski,[a] Kamil Sobczak,[b] Milena Ojrzyńska,[c] Dariusz Moszyński[d] and Wioletta Raróg-Pilecka[a]

Received 31st December 2025,
Accepted 18th May 2026

DOI: 10.1039/d5cy01610j

rsc.li/catalysis

Ammonia synthesis under mild reaction conditions remains a key challenge to realising a carbon-free society. The development of efficient catalysts for ammonia synthesis is therefore of great interest nowadays. Here, the effects of the cobalt deposition method and loading on the physicochemical properties and catalytic performance of Sm-doped $BaCeO_3$-supported Co catalysts were systematically investigated. Catalysts were prepared by deposition–precipitation, wet impregnation, and physical mixing methods. Depending on the method used, the catalyst properties varied in terms of chemisorptive properties and catalytic activity. The favourable activity observed for catalysts prepared by deposition–precipitation and wet impregnation methods was attributed to a more diverse surface landscape that facilitates hydrogen and nitrogen adsorption and activation. Then, by using the deposition–precipitation method, a series of catalysts with Co loadings from 10 to 50 wt% was synthesised. Catalytic testing revealed a clear dependence of activity on Co loading, with the highest reaction rate and intrinsic turnover frequency observed for the catalyst loaded with 40 wt% Co. This behaviour was explained not only by the greater number of adsorption sites but also by the structural sensitivity of cobalt in ammonia synthesis, where a diverse surface landscape with various adsorption sites improved the catalytic performance.

1. Introduction

Ammonia (NH_3) is one of the most important industrial chemicals, needed for fertiliser production and increasingly recognised as a promising hydrogen carrier and carbon-free fuel. This is due to the high energy density (12.8 GJ m^{-3}), high hydrogen content (17.8 wt%), liquefaction at room temperature and well-established transportation/storage technology. However, the industrial Haber–Bosch process, crucial for global ammonia synthesis, requires harsh reaction conditions (400–500 °C, 15–30 MPa) and consumes nearly 2% of the world's energy, accounting for roughly 1.8% of anthropogenic CO_2 emissions. The drive towards carbon neutrality and reduced energy demands has therefore stimulated efforts to develop catalysts that enable ammonia synthesis under milder, more sustainable conditions.[1–8]

The key challenge in ammonia synthesis lies in the activation of the stable nitrogen molecule (N≡N bond, 941 kJ mol^{-1}).[1] This requires a catalyst with a catalytic site with suitable electronic properties to weaken the N≡N triple bond. Conventional iron-promoted catalysts, although robust, require harsh operating conditions to achieve sufficient reaction rates, resulting in high energy costs and environmental impacts to meet ammonia demands. The development of new catalysts capable of operating under milder conditions offers a promising approach to mitigating the energy crisis and environmental issues.

Ruthenium catalysts supported on various oxides, such as MgO, CeO_2, La_2O_3, Pr_2O_3, and ZrO_2, have demonstrated enhanced activity at lower temperatures and pressures due to favourable nitrogen adsorption and dissociation properties.[1,9–15] However, the high cost and scarcity of ruthenium limit its industrial application, but at the same time, have prompted extensive research into alternative catalysts based on cobalt. Cobalt offers a promising alternative due to its lower price, higher abundance, and also comparable electronic configuration to iron.[16–28] However, pure cobalt exhibits limited activity due to the moderate nitrogen adsorption energy on its surface.[18] The performance of cobalt catalysts can be significantly improved by the choice

[a] Warsaw University of Technology, Faculty of Chemistry, Noakowskiego 3, 00-664 Warsaw, Poland. E-mail: hubert.ronduda@pw.edu.pl; Tel: +48 22 234 7602
[b] University of Warsaw Biological and Chemical Research Centre, Żwirki i Wigury 101, 02-089 Warsaw, Poland
[c] Institute of Optoelectronics, Military University of Technology, Kaliskiego 2, 00-908 Warsaw, Poland
[d] Faculty of Chemical Technology and Engineering, Department of Inorganic Chemical Technology and Environment Engineering, West Pomeranian University of Technology in Szczecin, Piastów Ave. 42, 71-065 Szczecin, Poland

of support, the cobalt deposition method, and the cobalt loading, which determine dispersion, the electronic environment, and the availability of active sites.[16–28] Support materials play an important role in determining the physicochemical properties of supported cobalt catalysts.[29] In particular, perovskite-type oxides, such as barium cerate ($BaCeO_3$) and barium zirconate ($BaZrO_3$), have emerged as attractive supports due to their high thermal stability, abundant oxygen vacancies and strong basicity. Moreover, the perovskite structure can be modified through cation substitution, allowing for the fine-tuning of electronic and acid–base properties. Recently, we demonstrated that cobalt catalysts supported on REE-doped $BaCeO_3$ perovskites (REE = Nd, Sm, and Gd) exhibited significantly enhanced ammonia synthesis activity, owing to optimised dopant incorporation that increases electron density and facilitates electron transfer from the support to cobalt, thereby promoting N_2 activation.[22] Also, studies on Ru-based catalysts have shown that REE-doped $BaCeO_3$ (REE = La, Y, and Pr) supports enhance catalytic activity by improving electron transfer, strengthening metal–support interactions (MSI), and increasing active-site stability.[10] In addition to the choice of support, the method used to introduce the active metal is crucial in determining dispersion, particle size, and the interaction strength between the metal and the support.[29] Among the most common techniques are wet impregnation (WI) and deposition–precipitation (DP). Wet impregnation (WI) is widely used because of its simplicity and controllable metal loading.[29–31] A metal precursor solution fills the pores of the support, and upon drying and calcination, the dispersed metal species can be distributed on the support. However, the uniformity of metal dispersion depends strongly on the support textural properties, and agglomeration and/or sintering phenomena may occur during calcination and/or reductive activation.[29–31] This can be especially problematic when the support surface area is low and high metal loadings are required. Deposition–precipitation (DP) typically provides a fine metal dispersion by precipitating metal hydroxides or carbonates directly on the support surface through pH-controlled precipitation.[29,32] This method favours the metal–support interaction and abundant active sites for catalytic reactions. These preparation routes strongly influence catalyst morphology, electronic structure, and reducibility.[29,32] For instance,[24] cobalt catalysts prepared by wet impregnation exhibited superior activity in ammonia synthesis compared to those prepared by deposition–precipitation, mainly due to the formation of cobalt nanoparticles (NPs) with an optimal size, thereby providing active sites with favourable chemisorptive properties. The method of cobalt deposition can therefore determine not only the extent of dispersion but also the nature of the active sites responsible for hydrogen and nitrogen activation.

Another important catalyst design aspect is the optimisation of metal loading, which affects both the size and dispersion of nanoparticles, as well as the chemisorptive properties of the active sites. At low metal loadings, metal is typically well-dispersed, leading to strong metal–support interactions (SMSI) and a high turnover frequency per surface atom. Increasing metal loading increases the number of accessible active sites, but can also promote particle agglomeration, thereby decreasing the effective surface area available for the catalytic reaction.[29] Studies on supported cobalt catalysts indicated that ammonia synthesis activity increased with cobalt loading up to 40 wt%, but higher loadings led to decreased activity due to excessive sintering.[33] Moreover, the changes in metal loading can alter the electronic environment of cobalt, thereby modifying its intrinsic catalytic activity. Indeed, ammonia synthesis is a structure-sensitive reaction in which the activity depends strongly on the structure and size of metal particles.[34] Among its two allotropic forms, hexagonal close-packed (hcp) cobalt is generally more active for ammonia synthesis than face-centred cubic (fcc) cobalt,[35] but the hcp–fcc phase balance depends on preparation and thermal treatment conditions and varies with cobalt size and structure.[36,37]

Despite considerable advances in cobalt catalysis, further research is needed to develop efficient catalysts for ammonia synthesis. Therefore, it is essential to adopt a rational design strategy to enhance the catalyst performance under milder reaction conditions. The present work aims to design an efficient supported cobalt catalyst for ammonia synthesis by systematically elucidating the interplay between cobalt deposition method, cobalt loading, and surface structure–activity relationships. Sm-doped $BaCeO_3$, a perovskite-type oxide, was used as the support, as it has been previously demonstrated to be highly effective for Co-based ammonia synthesis catalysts.[22] Detailed structural and surface characterisations, including N_2 physisorption, X-ray diffraction (XRD), scanning transmission electron microscopy (STEM), and temperature-programmed desorption (TPD), were complemented by catalytic testing. The findings are expected to contribute to the rational design of efficient cobalt ammonia synthesis catalysts operating under milder conditions, thereby emerging as an alternative to the commercial Fe-based catalysts.

2. Experimental section

2.1. Chemicals

All chemicals used were of analytic grade purity obtained from Merck, Acros Organics, or Chempur. Deionised water was used to prepare all aqueous solutions.

2.1.1. Support preparation. $BaCe_{0.9}Sm_{0.1}O_{3-\delta}$ (BCS) was used as a support for the preparation of cobalt catalysts. BCS was selected based on our previous work.[22] The support was prepared by a co-precipitation method.[22] Proper amounts of $Ba(NO_3)_2$, $Ce(NO_3)_3{\cdot}6H_2O$, and $Sm(NO_3)_3{\cdot}6H_2O$ were dissolved in deionised water under stirring and heated to 90 °C. Then, the double access of $(NH_4)_2CO_3$ solution was added dropwise.

The thus-obtained precipitate was aged at 90 °C for 1 h, then cooled, filtered, washed with deionised water and dried at 90 °C for 24 h. Finally, the sample was calcined at 1100 °C for 10 h.

2.1.2. Catalyst preparation by deposition–precipitation. A proper amount of $Co(NO_3)_2{\cdot}6H_2O$ was dissolved in deionised water under stirring. Cobalt loading was fixed at 10 wt%. Then, the BCS support was added to the solution under stirring, and the suspension was heated to 90 °C. Then, the K_2CO_3 solution was added dropwise until the pH reached 9. The thus-obtained precipitate was aged at 90 °C for 1 h, then cooled, filtered, and washed with deionised water until the conductivity was below 100 μS cm^{-1}. The obtained solid was then dried at 120 °C for 12 h and calcined at 500 °C for 5 h. The sample was denoted as 10Co-DP. Catalysts with the higher cobalt loadings of 20, 30, 40, and 50 wt% were also prepared using the above procedure and labelled as 20Co-DP, 30Co-DP, 40Co-DP, and 50Co-DP, respectively.

2.1.3. Catalyst preparation by wet impregnation. A proper amount of $Co(NO_3)_2{\cdot}6H_2O$ was dissolved in deionised water under stirring at room temperature. Cobalt content was fixed at 10 wt%. Then, the BCS support was added to the above solution, and the suspension was stirred for 15 min and kept overnight. The aqueous solvent was removed using a rotary evaporator at 60 °C and 200 mbar. The obtained solid was then dried at 120 °C for 12 h and calcined at 500 °C for 5 h. The sample was denoted as 10Co-WI. A catalyst with a higher cobalt loading of 30 wt% was also prepared using the above procedure and labelled as 30Co-WI.

2.1.4. Catalyst preparation by physical mixing. The proper amounts of Co_3O_4 and the BCS support were physically mixed using an agate mortar and pestle. Cobalt content was fixed at 10 wt%. The sample was denoted as 10Co-PM.

All the as-prepared catalysts were pelletised, crushed and sieved to 30–50 mesh before catalytic testing and characterisation. The reductive activation was typically carried out at 600 °C in a hydrogen-rich mixture to ensure the complete reduction of the Co precursor into metallic Co. Unless otherwise specified (*e.g.*, as-prepared catalyst, pre-catalyst), the catalysts mentioned in the paper refer to the reduced catalysts.

2.2. Characterisation methods

2.2.1. Inductively coupled plasma mass spectrometry (ICP-MS). Co metal loadings in catalysts were determined after microwave-assisted digestion using the M6 microwave digestion system (Preekem Scientific, Altium, Poland). Specifically, 6 mL of HNO_3 and 2 mL of HCl were added to approximately 30 mg of catalyst. Each sample was prepared in triplicate. The digestion program consisted of a 10 min ramp to 130 °C, a 3 min hold at 130 °C, an 8 min ramp to 180 °C, and a 15 min hold at 180 °C. After digestion, the samples were cooled to room temperature and then diluted with ultrapure water to a final volume of 25 mL. Before the ICP-MS analysis, the samples were diluted 1000-fold using 2% HNO_3 (v/v). The determination of total cobalt content was conducted using an Agilent ICP-MS 7850 (Agilent Technologies, Germany) instrument equipped with Agilent SPS4 Autosampler. Cobalt calibration standards in the range 2 to 1200 μg L^{-1} were prepared and analysed for quantification of Co by external calibration, with the addition of 2 μg L^{-1} yttrium as an internal standard to monitor plasma fluctuations and compensate for sensitivity shifts. The Co metal loadings were calculated as the mean value from the three replicates for each catalyst.

2.2.2. Hydrogen temperature programmed reduction (H_2-TPR). Hydrogen temperature-programmed reduction (H_2-TPR) studies were conducted using a Micromeritics AutoChem II 2920 chemisorption analyser equipped with a mass spectrometer (MKS Cirrus 200 AMU). A pre-catalyst sample (0.2 g) was placed in a U-shaped quartz reactor and heated to 800 °C at a ramp rate of 5 °C min^{-1} under a 10% H_2/Ar flow (40 mL min^{-1}). Hydrogen consumption during the reduction process was continuously monitored using a mass spectrometer at m/z = 2.

2.2.3. N_2 physisorption. N_2 physisorption measurements were conducted using a Micromeritics ASAP 2020 instrument at −196 °C. A pre-catalyst sample (0.5 g) was reduced *in situ* at 600 °C for 12 h under a H_2 flow (40 mL min^{-1}), followed by purging at 620 °C for 2 h under a He flow (40 mL min^{-1}). The catalyst was subsequently degassed under vacuum at 200 °C for 2 h, and the adsorption isotherms in the relative pressure (P/P_0) range of 0.05–0.3 were measured and analysed by using the BET method.

2.2.4. Thermogravimetric analysis (TGA). Thermogravimetric analysis (TGA) was employed to investigate the reduction/oxidation processes, and the TG curves were recorded using a Netzsch STA449C thermal analyser. A pre-catalyst sample (0.1 g) was heated from 30 to 600 °C with a ramp rate of 5 °C min^{-1} in a 50 vol% H_2/Ar flow (100 mL min^{-1}), held at 600 °C for 5 h and then cooled to 30 °C under an Ar flow (100 mL min^{-1}). The sample was then heated from 30 to 600 °C at a rate of 5 °C min^{-1} under a 10% O_2/N_2 flow (100 mL min^{-1}), held at 600 °C for 5 h, and then cooled to 30 °C.

2.2.5. Raman spectroscopy. Raman spectra were collected using a Renishaw inVia spectrometer with a 532 nm laser source, producing a ~1 μm spot at 1.95% power (~16 mW). The experiments were carried out at room temperature. Mapping mode was applied over an area of approximately 20 μm × 20 μm, yielding around 400 spectra for 2 s at each spot. Raman spectra were collected at different laser powers (1–10%, ~8–80 mW) for 5 s each, and the measurement spot was changed after each acquisition to eliminate the effect of laser-induced heating at a given location on the sample. Individual bands were fitted with a Lorentzian function, and the uncertainties were determined using the least-squares method in Origin2025. The maps were generated by extracting the intensity at 348 cm^{-1} and by

determining the maximum intensity of the A_{1g} mode in the WiRE software.

2.2.6. X-ray powder diffraction (XRD). X-ray diffraction (XRD) analysis was performed on a Bruker D8 Advance diffractometer with Cu-Kα radiation (λ = 0.15418 nm) operated at 40 kV and 40 mA. XRD patterns for the pre-catalysts were acquired without pre-treatment, whereas XRD patterns for the catalysts were collected after *ex situ* reduction at 600 °C for 24 h under a H_2 flow (40 mL min^{-1}). XRD patterns were recorded in the Bragg–Brentano (θ/θ) horizontal geometry over a 2θ range of 10° to 90° in a continuous scan mode, with a step size of 0.03° and a counting time of 10 s per step.

2.2.7. Scanning transmission electron microscopy with energy-dispersive X-ray spectroscopy (STEM-EDX). Microscopic observations were conducted on a Talos F200X (FEI) microscope in scanning transmission electron microscopy (STEM) mode, equipped with a high-angle annular dark-field (HAADF) detector and an energy-dispersive X-ray (EDX) spectrometer (Bruker BD4 spectrometer). The images were collected after *ex situ* reduction at 600 °C for 24 h under a H_2 flow (40 mL min^{-1}). The sample was then dispersed in ethanol under ambient conditions, and a few drops of the dispersion were placed on a carbon-coated copper mesh TEM grid. The grid was left to dry overnight at room temperature. Particle sizes were determined exclusively for Co, despite the presence of other elements (Ba, Ce) in the analysed sample. To ensure their unambiguous identification, a combination of HAADF-STEM imaging and EDX mapping was employed. The cobalt distribution maps were overlaid onto the corresponding HAADF images, which, despite the inherent broadening of the EDX signal, enabled precise identification of Co particles contours and elimination of contributions from Ba and Ce. The identified cobalt particles were manually outlined, and the resulting data were used to construct particle-size distribution histograms.

2.2.8. H_2 temperature-programmed desorption (H_2-TPD). H_2 temperature-programmed desorption (H_2-TPD) experiments were also performed using the same equipment as for TPR measurements. A pre-catalyst sample (0.5 g) was subjected to *in situ* reduction at 550 or 600 °C under a H_2 flow (40 mL min^{-1}) for 12 h, followed by purging at 570 or 620 °C under an Ar flow (40 mL min^{-1}) for 2 h, and cooled to 150 °C. The sample was then exposed to a H_2 flow (40 mL min^{-1}) for 15 min, followed by further cooling to 0 °C and holding at that temperature for an additional 15 min. The system was then purged with Ar for 1 h. The TPD process was carried out under an Ar flow (40 mL min^{-1}) at ramp rates of 5, 10, 15, and 20 °C min^{-1}, reaching 600 °C, during which the H_2 signal (m/z = 2) was continuously monitored by a mass spectrometer. The quantity of desorbed hydrogen per unit mass of the catalyst was calculated with an experimental error margin of ±5%.

2.2.9. N_2 temperature-programmed desorption (N_2-TPD). N_2 temperature-programmed desorption (N_2-TPD) experiments were also performed using the same equipment as for TPR measurements. A pre-catalyst sample (0.5 g) was subjected to *in situ* reduction at 600 °C under H_2 flow (40 mL min^{-1}) for 12 h, followed by purging at 620 °C for 2 h under a He flow (40 mL min^{-1}), and cooled to 200 °C. The sample was then exposed to an N_2 flow (40 mL min^{-1}) for 4 h, followed by further cooling to 0 °C. The system was then purged with He for 1 h. The TPD process was carried out under a He flow (40 mL min^{-1}) at a ramp rate of 10 °C min^{-1}, reaching 600 °C, during which the N_2 signal (m/z = 28) was continuously monitored by a mass spectrometer. The quantity of desorbed nitrogen per unit mass of the catalyst was calculated with an experimental error margin of ±5%.

2.2.10. CO_2 temperature-programmed desorption (CO_2-TPD). CO_2 temperature-programmed desorption (CO_2-TPD) experiments were also performed using the same equipment as for TPR measurements. A pre-catalyst sample (0.5 g) was subjected to *in situ* reduction at 600 °C under a H_2 flow (40 mL min^{-1}) for 12 h, followed by purging at 620 °C under a He flow (40 mL min^{-1}) for 2 h. After cooling to 40 °C, the sample was exposed to CO_2 (40 mL min^{-1}) for 2 h. The system was then purged with He for 1 h. The TPD process was carried out under a He flow (40 mL min^{-1}) at a ramp rate of 10 °C min^{-1}, reaching 700 °C, during which the CO_2 signal (m/z = 44) was continuously monitored by a mass spectrometer.

2.2.11. X-ray photoelectron spectroscopy (XPS). The surface composition of the selected catalyst was analysed using X-ray photoelectron spectroscopy (XPS). A PREVAC electron spectrometer equipped with a Scienta SES 2002 electron energy analyser was used. The data were acquired in a high-resolution mode, with a pass energy of 50 eV. An X-ray tube with an aluminium anode, generating radiation with an energy of 1486.6 eV, was used. A correction of the binding energy was performed due to the presence of the surface charging effect. It was assumed that the Ba 4d spectral line corresponding to oxidised barium atoms is located at a binding energy of 89.2 eV.[38]

2.3. Catalytic activity tests

The ammonia synthesis reaction was performed in a tubular flow reactor. A detailed experimental setup is described in our previous works.[39,40] The methodology employed in this study excluded mass transfer limitations, ensuring that the reaction proceeds in the kinetic regime.[39,40] A pre-catalyst sample (0.5 g) was activated according to the following temperature protocol: 470 °C for 72 h, 520 °C for 24 h, 550 °C for 48 h, and 600 °C for 24 h. The activation process was carried out in a H_2/N_2 flow ($H_2:N_2$ = 3 : 1, 70 L h^{-1}). Next, the reactor was pressurised to 6.3 MPa and cooled to 470 °C. The measurements were performed under steady-state conditions, and ammonia produced during the reaction was analysed interferometrically. The catalyst bed temperature was measured using a thin thermocouple positioned axially in a steel sheath. The axial temperature profiles were measured, and the average catalyst bed temperature was determined. The ammonia synthesis rate was calculated using the mass

balance for a plug-flow differential reactor. The average error in the determination of ammonia synthesis rate was ±1%. The turnover frequency (TOF) was calculated by dividing the ammonia synthesis rate by the number of surface cobalt atoms. The number of surface cobalt atoms was estimated from H_2-TPD experiments, assuming a stoichiometry of H/Co = 1.[41] The thermal stability of the catalyst was evaluated by repeating the catalytic tests at 470 °C and 6.3 MPa after catalyst overheating at 600 °C for 24, 48, and 72 h under atmospheric pressure.

3. Results and discussion

3.1. Studies on the effects of the Co deposition methods

First, we examined the influence of the Co deposition method on the properties of the cobalt catalysts prepared by deposition–precipitation, wet impregnation, and physical mixing. This approach enables a direct comparison of how the Co deposition strategy governs cobalt dispersion, metal–support interactions, chemisorptive properties and the catalytic performance. The results of the ammonia synthesis reaction carried out over 10Co-DP, 10Co-WI, and 10Co-PM are shown in Fig. 1.

The catalyst performance varied depending on the method used for Co deposition. The highest ammonia synthesis rate of 2.21 g_{NH_3} g_{cat}^{-1} h^{-1} was noted for the 10Co-WI catalyst, which was about 1.4 times that of 10Co-DP (1.56 g_{NH_3} g_{cat}^{-1} h^{-1}) and 2.9 times that of 10Co-PM (0.75 g_{NH_3} g_{cat}^{-1} h^{-1}). In the case of intrinsic activity (TOF), the highest TOF values of 0.260 s^{-1} and 0.251 s^{-1} were observed for 10Co-DP and 10Co-WI, respectively. For 10Co-PM, the TOF value (0.166 s^{-1}) was about 1.5 times lower than that of 10Co-DP and 10Co-WI. These results suggest that the reaction rate over 10Co-DP and 10Co-WI is determined by the number of available active sites, as almost the same TOF values were observed. For 10Co-PM, in turn, the low ammonia synthesis rate suggests that it is influenced not only by the number of available active sites, but also by the intrinsic activity of the cobalt sites. The TOF values reflect the intrinsic properties of cobalt, while the ammonia synthesis rate is constrained by the number and activity of reaction sites. To elucidate the origins underlying the catalytic performance disparity, detailed structural, morphological, and surface characterisation investigations were employed.

Co metal loadings were determined by ICP-MS, providing composition information for the bulk of the catalysts (Table S1). The Co loadings in the catalysts correspond well to the nominal values, indicating successful Co deposition. All the catalysts exhibited poor porosity. The BET surface areas were 4.5, 4.9, and 4.5 m^2 g_{cat}^{-1} for 10Co-DP, 10Co-WI, and 10Co-PM, respectively. Such a low surface area is due to the low surface area of the BCS support material (4.3 m^2 g^{-1} (ref. 22)), preventing a well-controlled metal distribution.

Using XRD, the catalyst structures were analysed and compared (Fig. S1). The diffraction peaks attributable to the

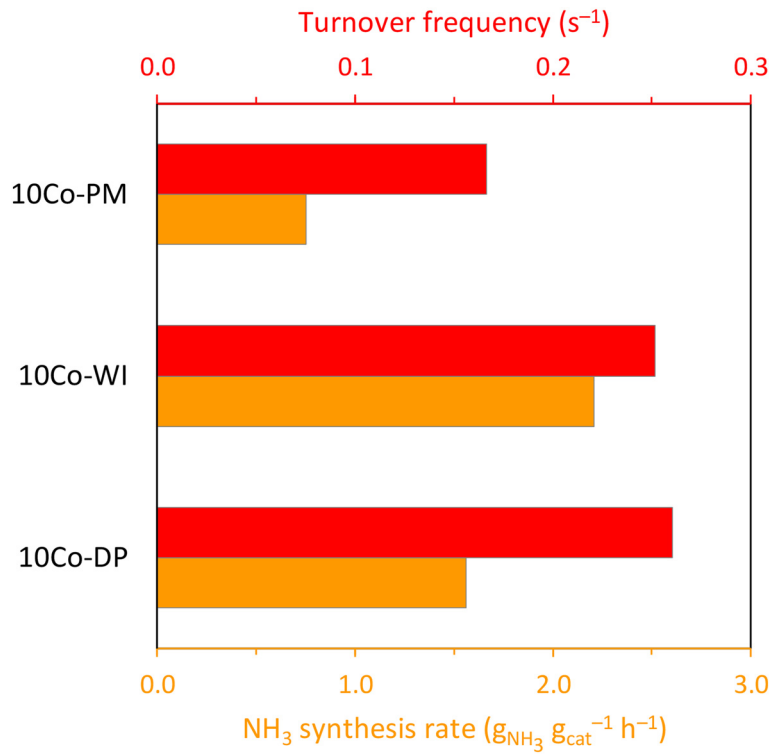

Fig. 1 Ammonia synthesis activity over cobalt catalysts obtained by different cobalt introduction methods. The activity was expressed as ammonia synthesis rate (orange bars) and turnover frequency (red bars). Reaction conditions: pressure, 6.3 MPa; temperature, 470 °C; synthesis gas, H_2/N_2 = 3 with a flow rate of 70 L h^{-1}.

$BaCeO_3$ orthorhombic structure (*Pmcn* space group) were observed, with no peaks related to the Sm-containing phase, confirming the successful incorporation of the Sm dopant into the $BaCeO_3$ support lattice.[22] There were also peaks at 44.2°, 51.5°, and 75.9°, ascribable to the face-centred cubic (fcc) Co phase (PDF 15-0806), corresponding to the (111), (200), and (220) lattice planes, respectively. This indicates the complete reduction of deposited Co metal species to metallic Co; the Co crystallite sizes were 29, 25, and 33 nm for 10Co-DP, 10Co-WI, and 10Co-PM, respectively. The negligible peaks ascribable to the barium carbonate were also seen.

HAADF-STEM images and EDX elemental mapping of the main catalyst components (Co, Ba, Ce) are shown in Fig. S2. For all the catalysts, the EDX maps of Ba overlap with Ce, showing no distinct particles containing separate Ba or Ce phases. For 10Co-DP and 10CoWI, the Co nanoparticles were relatively spherical and evenly distributed across the support; however, agglomeration of Co was observed. The size of these agglomerated particles varied from 50 to 150 nm. It appears that the Co NPs were more agglomerated in 10Co-DP than in 10Co-WI. For the 10Co-PM catalyst, the images clearly revealed a strong agglomeration of Co NPs. The Co NPs consisted of dense agglomerates of various shapes, with sizes ranging from 50 to 500 nm.

Hydrogen temperature-programmed desorption (H_2-TPD) analyses were conducted to characterise the surface heterogeneity of Co dispersed over the BCS support. Fig. 2 presents the hydrogen TPD profiles of the catalysts. The m/z = 2 signal, attributed to H_2, was continuously monitored during the desorption step. Two distinct desorption peaks were observed at 100–200 °C and 400–600 °C for all catalysts, indicating the presence of hydrogen adsorption sites with different binding energies. The low-temperature peak (LT) is ascribed to the desorption of hydrogen that weakly binds to the Co sites, whereas the high-temperature peak (HT) is associated with the strong chemisorption state of hydrogen on the Co sites.[42,43] In general, similar hydrogen desorption behaviour was observed across all catalysts; however, for 10Co-PM, the HT desorption peak was relatively broad and shifted to higher temperatures.

The amount of H_2 desorbed, calculated by integrating the area under the desorption curves, was used to quantify the hydrogen adsorption sites (Table S2). The 10Co-WI catalyst exhibited improved hydrogen chemisorption capacity compared to the 10Co-DP and 10Co-PM; the total H_2 chemisorption was about 1.5 times that of 10Co-DP and 1.9 times that of 10Co-PM. The ratio of the low-temperature peak to the high-temperature peak (LT/HT ratio) was calculated and used as a measure of heterogeneity in hydrogen adsorption sites (Table S2). It indicates the proportion of weak hydrogen-binding sites to strong hydrogen-binding sites. It has been reported that the presence of weak and strong binding sites in a similar proportion creates a more diverse surface landscape, facilitating dissociative hydrogen adsorption and subsequent reaction with nitrogen to form ammonia.[24] The predominance of only weak or strong hydrogen adsorption sites is deemed undesirable because it either binds hydrogen too weakly or too strongly, leading to the blockage of active sites and a loss of catalytic activity.[24] It is suggested that 10Co-WI and 10Co-DP possess a more

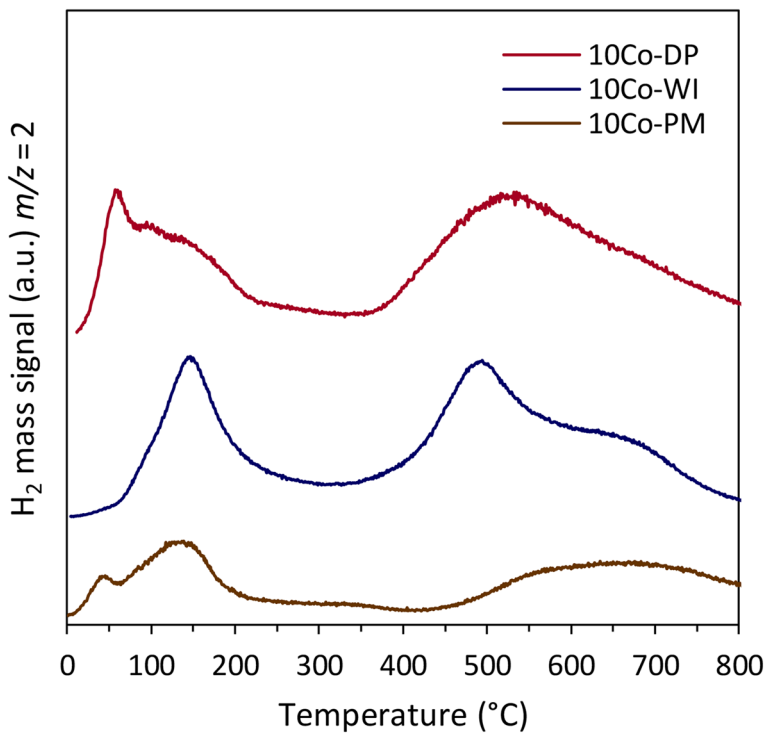

Fig. 2 H_2-TPD analyses of the 10Co-DP, 10Co-WI, and 10Co-PM catalysts.

diverse surface landscape than 10Co-PM, because the calculated LT/HT ratio is closer to 1.[24] The high hydrogen chemisorption capacity of the 10Co-WI catalyst, with its diverse surface landscape featuring various adsorption sites, is supposed to contribute to the enhanced rate of ammonia synthesis. These results highlight the crucial role of the metal introduction method in controlling the size and distribution of the metal on the support. This, in turn, greatly affects interactions between the metal and the support, thereby tailoring the reactivity of the cobalt sites.

According to TPD theory, under the conditions that mass transfer limitations are negligible and re-adsorption can be excluded, the following equation can be used to calculate the H_2 desorption activation energy, as reported in ref. 42 and 43:

$$2\log T_m - \log\beta = \frac{E_d}{R}\frac{1}{T_m} + \log\frac{E_d}{AR}$$

where T_m is the temperature of the desorption peak maximum (K), β is the heating rate (K min^{-1}), E_d is the desorption activation energy (kJ mol^{-1}), and A is the desorption frequency factor.

Thus, from the slopes of the "$2\log T_m - \log\beta$" *versus* $1/T_m$ plots of the linear fit plots, E_d can be calculated.[43] The 10Co-WI and 10Co-DP catalysts were further studied to gain insight into the desorption property of hydrogen species from the active sites (Fig. 3).

The activation energies for H_2 desorption at low-temperature desorption peaks were 40.2 and 91.8 kJ mol^{-1} for 10Co-DP and 10Co-WI, respectively. At the high-temperature region, the hydrogen desorption activation energies were 168.1 and 129.6 kJ mol^{-1}. These results confirm that the deposition method not only affects the Co size and distribution but also influences the nature and strength of interactions with hydrogen. For 10Co-WI, the stronger intrinsic hydrogen adsorption on Co was observed at the low-temperature region, whereas at the high-temperature region, the stronger hydrogen chemisorption was observed for 10Co-DP. These differences can be attributed to differences in the properties of cobalt, such as size and structure. Indeed, it has

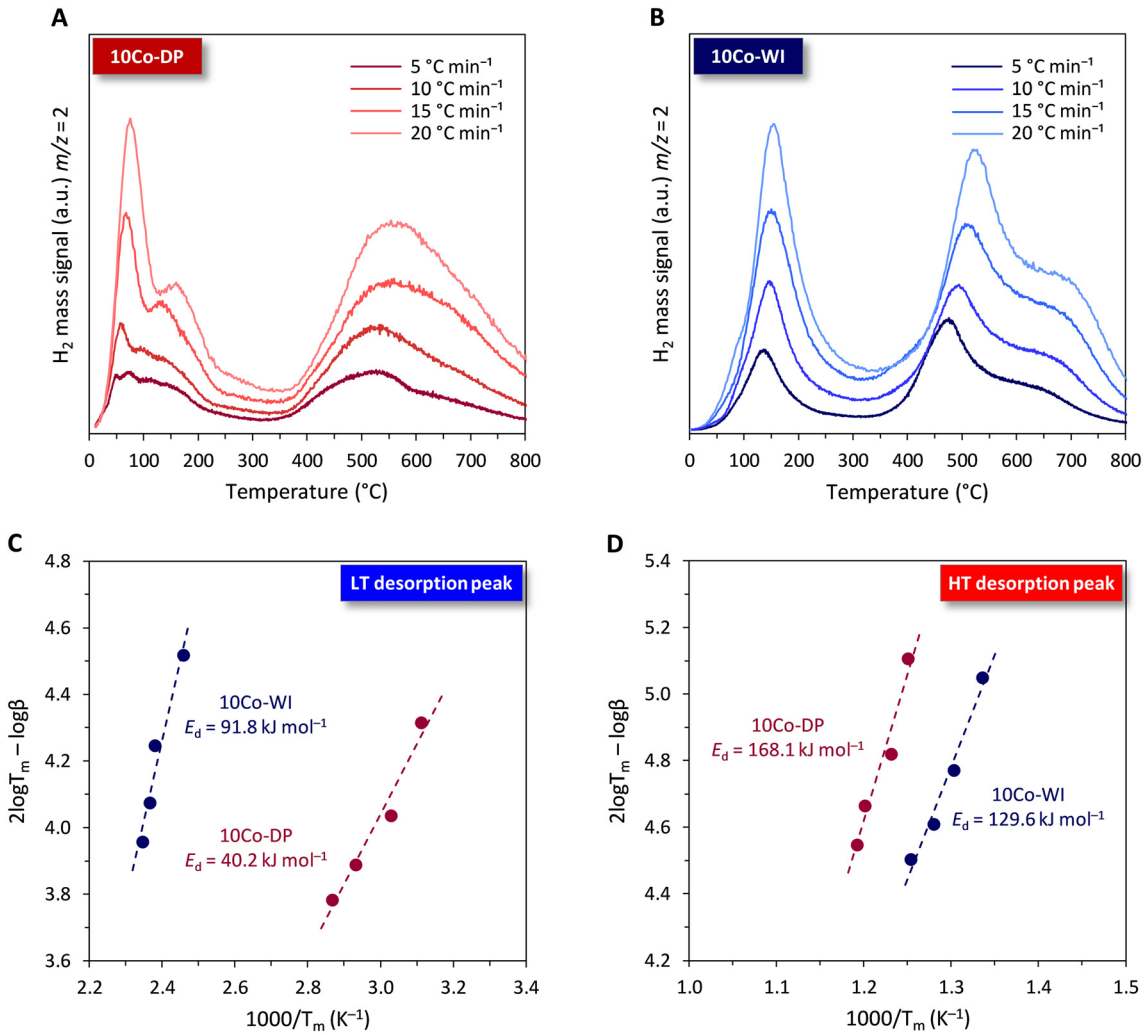

Fig. 3 H_2-TPD analyses for the (A) 10Co-DP and (B) 10Co-WI catalysts with different temperature ramp rates, and the respective activation energies for H_2 desorption at the (C) low-temperature and (D) high-temperature regions.

been reported that adsorption and desorption of hydrogen and nitrogen depend on the structure of Co,[18,44,45] thus affecting the catalytic behaviour of cobalt.

To summarise this section, it is confirmed that the method of cobalt deposition influences the catalyst properties and performance. A particularly high ammonia formation rate was observed for the catalyst obtained by the wet impregnation method. This resulted from its high hydrogen chemisorption capacity and a diverse surface landscape with various adsorption sites. The lower ammonia formation rate observed for the catalyst obtained by deposition–precipitation is attributed to the lower Co dispersion, as the 10Co-WI and 10Co-DP catalysts exhibited almost the same TOF values. Compared with 10Co-DP and 10Co-WI, the physically mixed catalyst (10Co-PM) exhibited the lowest catalytic activity due to severe agglomeration of Co NPs, leading to low Co dispersion, but also to the limited heterogeneity in adsorption sites.

3.2. Studies on the effects of the Co loading amounts

In the next stage, we examined the influence of Co loadings on the properties of the cobalt catalysts. The appropriate metal loading is crucial for maximising the availability of surface active sites, accounting for the ammonia synthesis reaction. Optimal metal loading is also important from a technological perspective; an appropriate activity-to-price ratio is crucial for developing efficient, cost-effective catalysts. Although the wet impregnation method was found to be the most suitable for Co deposition, it is often recognised as unsuitable for high metal loadings, especially on low-surface-area supports due to limited porosity, thus promoting excessive nanoparticle agglomeration during thermal treatment. In such cases, alternative deposition methods are required to achieve uniform metal distribution with controlled particle size.[29,30,32] To check this, we prepared catalysts loaded with 30 wt% Co using wet impregnation and deposition–precipitation, denoted as 30Co-WI and 30Co-DP, respectively. The results of the ammonia synthesis reaction carried out over 30Co-WI and 30Co-DP are shown in Fig. 4A. The ammonia synthesis rate of 30Co-DP reached 4.01 g_{NH_3} g_{cat}^{-1} h^{-1}, which was about 1.7 times that of 30Co-WI (2.82 g_{NH_3} g_{cat}^{-1} h^{-1}). The TOF value of 0.402 s^{-1} was observed for 30Co-DP, which was about 1.1 times that of 30Co-WI (0.356 s^{-1}). This suggests that the observed differences in ammonia formation rates are primarily due to differences in the number of available Co surface active sites.

To confirm this, the number of hydrogen adsorptive sites was determined by H_2-TPD (Fig. S3). The hydrogen chemisorption capacity of 30Co-WI was 26% lower than that of 30Co-DP (Table S3). Interestingly, the H_2 chemisorption of 30Co-WI was 11% lower than that of 10Co-WI (Tables S2 and S3). This decrease indicates severe sintering of Co NPs, leading to a decrease in the exposed Co atoms. Indeed, the BET surface area of 30Co-WI was 3.0 m^2 g^{-1}, about 1.6 times lower than that of 10Co-WI (4.9 m^2 g^{-1}). XRD confirmed the presence of fcc-Co with a crystallite size of 32 nm (Fig. S4), comparable to that of 10Co-WI, despite much higher Co loading. This observation is consistent with a previous report,[33] suggesting that, although the crystallite size remains similar, agglomeration increases with Co loading. Indeed, pronounced sintering and agglomeration of Co nanoparticles in 30Co-WI were confirmed by STEM-EDX analysis (Fig. S5).

Based on these findings, we selected the deposition–precipitation method for Co deposition, as it was shown to be suitable for high metal loadings. By modulating the Co loading, we prepared the catalysts loaded with 10, 20, 30, 40 and 50 wt% Co. The results of the ammonia synthesis reaction are displayed in Fig. 4. Fig. 4A shows the effect of Co loading on the ammonia synthesis performance. The ammonia synthesis rate gradually increased from 1.56 to 4.80 g_{NH_3} g_{cat}^{-1} h^{-1} as the Co loading increased from 10 to 40 wt%. A further increase in the Co loading from 40 to 50 wt% resulted in a slight decrease in the ammonia synthesis rate (4.47 g_{NH_3} g_{cat}^{-1} h^{-1}). The intrinsic activities (TOF) exhibited the same trend. The catalysts were also tested at different temperatures (400, 430, and 470 °C) (Fig. 4B). The resulting reaction rates were used for the Arrhenius plots in Fig. 4C. The determined apparent activation energies (E_a) were 74.2, 66.4, 59.0, 56.3, and 52.7 kJ mol^{-1} for 10Co-DP, 20Co-DP, 30Co-DP, 50Co-DP, and 40Co-DP, respectively. The lowest apparent activation energy of 40Co-DP suggests the presence of highly active surface Co sites, allowing efficient activation of N_2 and H_2 molecules. In addition, the ammonia synthesis stability tests were conducted (Fig. 4D). The catalysts were overheated at 600 °C for 72 h, and the reaction rates were measured at specific times (after 24, 48 and 72 h). Such a high temperature was intentionally chosen to accelerate possible thermally induced processes, such as sintering, and thus provide insight into the long-term thermal stability of the catalysts. The catalysts exhibited a slight decrease in ammonia synthesis rates of about 5%. This suggests that catalysts were rather stable under the applied reaction conditions. In the catalysts where sintering is severe, a more pronounced and continuous decline in performance would typically be expected due to the loss of active sites.

The ammonia synthesis performance of the catalysts was compared with that of other literature-reported supported catalysts (Table S4). Generally, the reaction rates obtained at 470 °C for our catalysts (Table S4, entries 29–33) are competitive with those reported in the literature. The reaction rates were higher than those for supported iron and ruthenium catalysts; however, the catalytic tests were performed under lower temperatures and pressures. Although a direct comparison was not possible due to the different reaction conditions, it is still possible to deduce that our catalysts show considerable potential. Under identical reaction conditions (Table S4, entries 19–33), our catalysts outperformed other supported cobalt catalysts, exhibiting at least a 2-fold higher reaction rate, thus highlighting the decisive role of the support. Notably, it achieves exceptionally high ammonia synthesis rates, surpassing not only

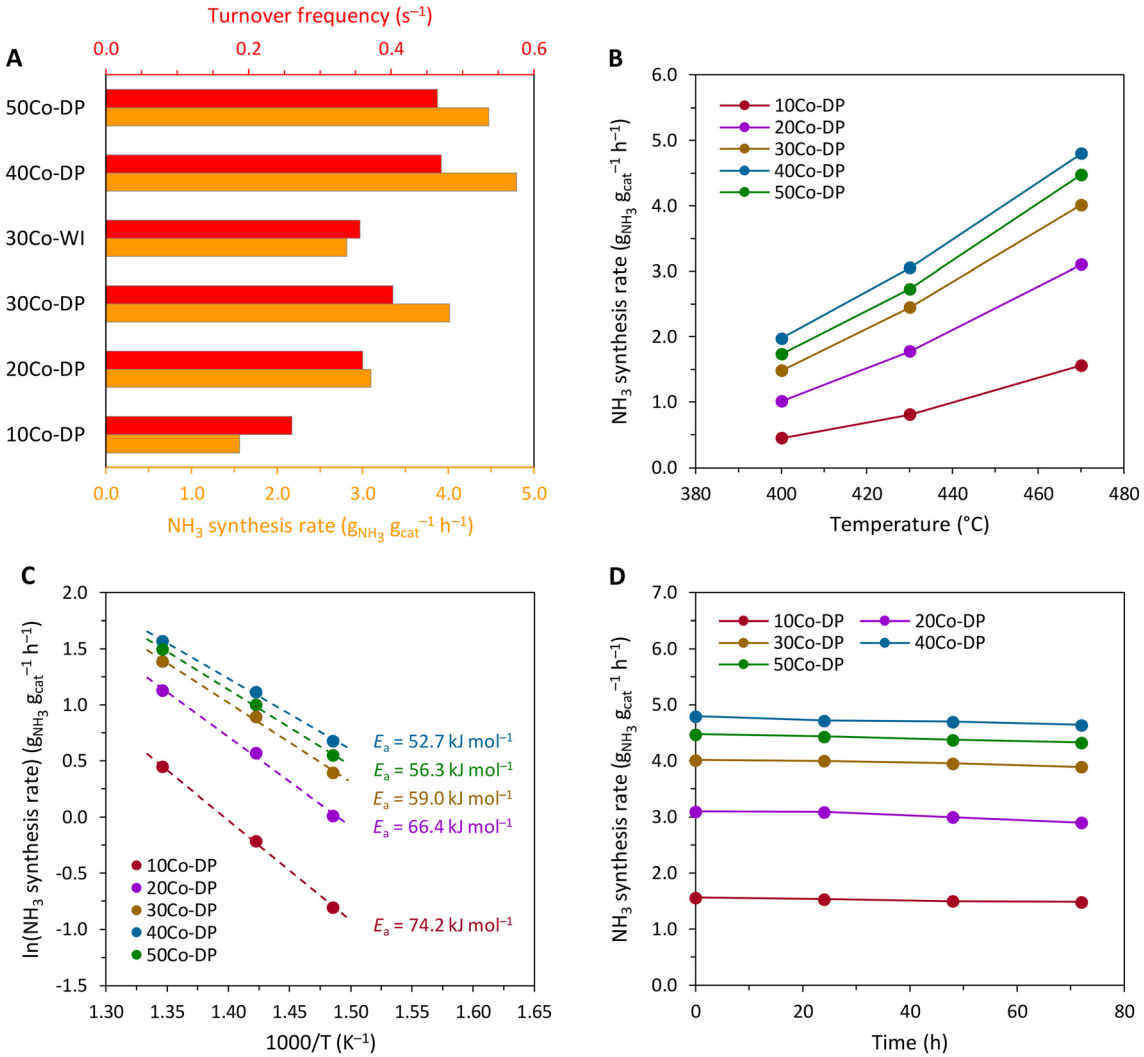

Fig. 4 Evaluation of the ammonia synthesis activities over the 30Co-WI and *x*Co-DP (*x* = 10, 20, 30, 40, and 50) catalysts. (A) Effect of Co loading amounts on the ammonia synthesis rate at 470 °C. (B) Temperature dependence of ammonia synthesis rate. (C) Arrhenius plots for ammonia synthesis reaction. (D) Time dependence of ammonia synthesis rate at 470 °C. Reaction conditions: pressure, 6.3 MPa; temperatures, 400–470 °C; synthesis gas, H_2/N_2 = 3 with a flow rate of 70 L h^{-1}.

conventional Co catalysts but also competing with industrial Fe catalysts (Table S5). Specifically, at 6.3 MPa and 400 °C, the ammonia synthesis rate per mass of catalyst over our catalyst was 1.4 times lower than that of KM1R (an industrial iron catalyst). However, when the reaction rate was expressed per unit mass of metal, the catalyst showed about 1.7 times the performance of KM1R, indicating better utilisation of the active metal species, and making our catalyst an attractive alternative.

A detailed investigation of the structure, morphology, and chemisorptive properties was conducted to understand the key factors affecting catalyst activity. First, the actual Co loadings were determined by ICP-MS (Table S1). The results revealed that the Co loadings were close to the nominal values, indicating successful Co deposition at different loadings using the deposition–precipitation method. H_2-TPR analysis was performed to study the reductive activation of the pre-catalysts. The TPR analyses are shown in Fig. 5. Hydrogen consumption was monitored by the *m*/*z* of 2. The observed peaks are associated with the reduction of the Co_3O_4 oxide, as XRD and Raman analyses identified Co_3O_4 in the pre-catalysts (Fig. S6–S8). The TPR curves exhibited two maxima, one at about 300 °C and the second at 400–450 °C. The low-temperature peak occurred at the same temperature for all the catalysts, whereas the high-temperature peak shifted towards higher temperatures for the high cobalt-loaded catalysts (≥30 wt% Co) (Fig. 8). Meanwhile, for the high-loaded cobalt catalysts, the second peak consisted of two overlapping peaks, indicating a different reductive process than that observed for low cobalt-loaded catalysts. In the case of 10Co-DP and 20Co-DP, the reduction of Co_3O_4 occurred in two stages.[46] The peak at 300 °C was assigned to the reduction of Co^{3+} to Co^{2+}, and the peak at 400 °C corresponded to the reduction of Co^{2+} to Co^0. For the 30Co-DP, 40Co-DP and 50Co-DP pre-catalysts, the Co_3O_4 reduction probably occurred in three stages. The peak at 300 °C was

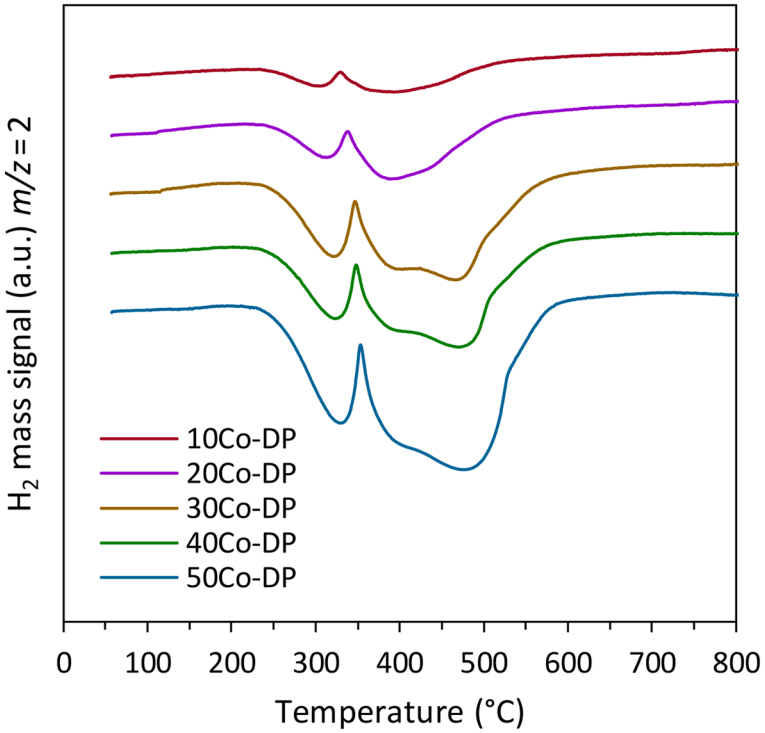

Fig. 5 H_2-TPR analyses of the *x*Co-DP (*x* = 10, 20, 30, 40, and 50) pre-catalysts.

attributed to the reduction of Co^{3+} to Co^{2+}, and the two overlapping peaks between 400 and 450 °C were due to the reduction of Co^{2+} to (Co^0Co^{2+}), and Co^{2+} to Co^0.[47] These results may suggest the presence of Co_3O_4 with different particle sizes and a broader size distribution than in the low cobalt-loaded catalysts. Indeed, in the literature, it is reported that the reduction of Co_3O_4 depends strongly on particle size and morphology, and that for larger Co_3O_4 particles, reduction occurs at higher temperatures.[48,49] H_2 consumption during the TPR analyses increased gradually with increasing cobalt loading (Table S6).

The thermogravimetric (TG) analysis was performed to study the reduction and oxidation processes. The obtained DTG curves are shown in Fig. S9, whereas the corresponding mass losses and mass gains are shown in Table S7. The DTG curves exhibited two sharp peaks at about 270 and 340 °C during the reduction step, suggesting a two-step reduction for all the pre-catalysts. Moreover, compared with the TPR profiles (Fig. 5), the peaks occurred at lower temperatures. This can be explained by the use of the H_2-rich mixture (50% H_2/Ar) during TGA experiments. This likely resulted in no visible overlap of the high-temperature peak in the high cobalt-loaded catalysts. During the oxidation step, a broad peak at about 340 °C, likely consisting of two peaks, was observed. This suggests that Co metal oxidation occurs in two steps: Co^0 to Co^{2+} and Co^{2+} to Co^{3+}. The recorded mass losses increased gradually with increasing Co loadings. During the oxidation step, a gradual increase in mass gain was observed with increasing Co content. The differences between the recorded mass losses and mass gains are due to the presence of moisture in the pre-catalysts, thus contributing to the higher mass loss. Generally, the TPR and TGA analyses also enabled the calculation of the Co loading in the catalysts. All three methods (ICP-MS, TGA, and TPR) showed consistent results (Tables S1, S6, and S7).

After *in situ* hydrogen treatment, the BET surface areas of the catalysts were determined (Table 1). All the catalysts exhibited poor porosity. The BET surface areas increased with

Table 1 Physicochemical properties of the *x*Co-DP (*x* = 10, 20, 30, 40, and 50) catalysts

Catalyst	BET surface area[a] ($m^2\ g_{cat}^{-1}$)	Co particle size[b] (nm)	Co crystallite size[c] (nm)
10Co-DP	4.5	36	29
20Co-DP	5.2	41	31
30Co-DP	6.4	42	30
40Co-DP	7.2	—	29
50Co-DP	7.0	—	30

[a] Determined by N_2 physisorption. [b] Determined by STEM-EDX. For the 40Co-DP and 50Co-DP catalysts, Co agglomeration was severe, making it difficult to determine a clear particle-size distribution. [c] Determined from the (111) reflection of the fcc-Co.

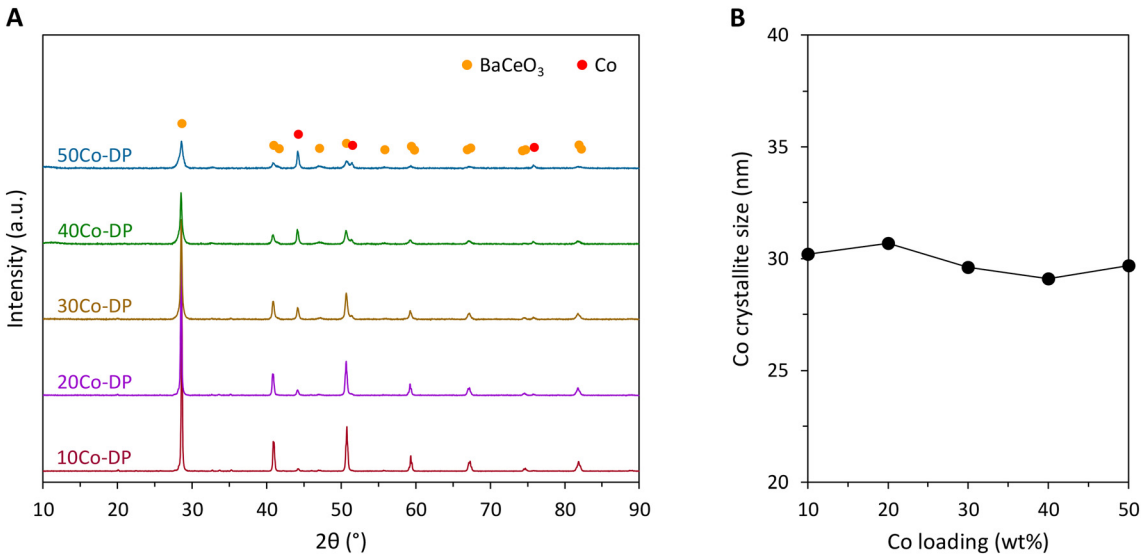

Fig. 6 (A) XRD patterns of the *x*Co-DP (*x* = 10, 20, 30, 40, and 50) catalysts. The orange dot (●) indicates $BaCeO_3$, and the red dot (●) indicates fcc-Co. (B) The dependence of Co loading amount on Co crystallite size.

increasing cobalt loading, reaching a maximum of 7.2 m^2 g_{cat}^{-1} at 40 wt% Co, then slightly decreased.

X-ray diffraction (XRD) was used to evaluate the catalyst structures, and the results are shown in Fig. 6. The strong diffraction peaks attributable to the $BaCeO_3$ orthorhombic structure were seen. There were also peaks at 44.2°, 51.5°, and 75.9°, ascribable to the face-centred cubic (fcc) Co phase (PDF 15-0806), corresponding to the (111), (200), and (220) lattice planes, respectively. In addition, a hexagonal close-packed (hcp) Co phase (PDF 01-1278) was likely to be present in high cobalt-loaded catalysts (≥30 wt% Co). However, the peaks of hcp-Co were very weak and partially overlaid with the reflections of other phases. This did not allow for the unequivocal determination of the presence of this phase. It is also observed that the intensity of diffraction reflections varied with increasing Co loading. The intensity of the diffraction peaks originating from the $BaCeO_3$ phase decreased while those originating from the Co metal increased. The presence of metallic Co with no reflections associated with Co oxides indicates the complete reduction of deposited Co oxide to metallic Co. The Co crystallite size was almost the same across all catalysts, ranging from 29 to 31 nm, as shown in Table 1 and Fig. 6B. This suggests that, despite increased cobalt loading, the Co crystallites did not grow and remained stable.

X-ray photoelectron spectroscopy (XPS) was used to examine the surface composition. The elements detected at the catalyst surface were barium, cerium, cobalt, and oxygen. Trace amounts of samarium as well as "adventitious carbon" were also observed. It is particularly significant that only trace amounts of samarium atoms are present on the surface of the catalysts. Rare-earth element (REE) atoms sometimes tend to accumulate on the surface of materials.[50] Therefore, the negligible presence of samarium in the spectra observed for the studied catalysts confirms the earlier conclusion, based on XRD studies, that these atoms have incorporated into the $BaCeO_3$ structure (Fig. 6). Due to the presence of both cobalt and barium in the catalysts, it was not possible to use the main cobalt spectral line, Co 2p, to determine the chemical state of cobalt atoms located on the catalyst surface. This is because of the overlap of the Ba 3d and Co 2p lines. For this reason, the XPS Co 3p line was used to determine the surface chemical state of cobalt. The results recorded for three catalysts are presented in Fig. 7. The intensity of the Co 3p line increased with increasing cobalt loading in the catalysts. This indicates that as cobalt loading increases, the catalyst surface becomes progressively enriched with cobalt. Analysis of the XPS Co 3p spectra indicates that after the reduction process, cobalt oxide initially present in the catalyst

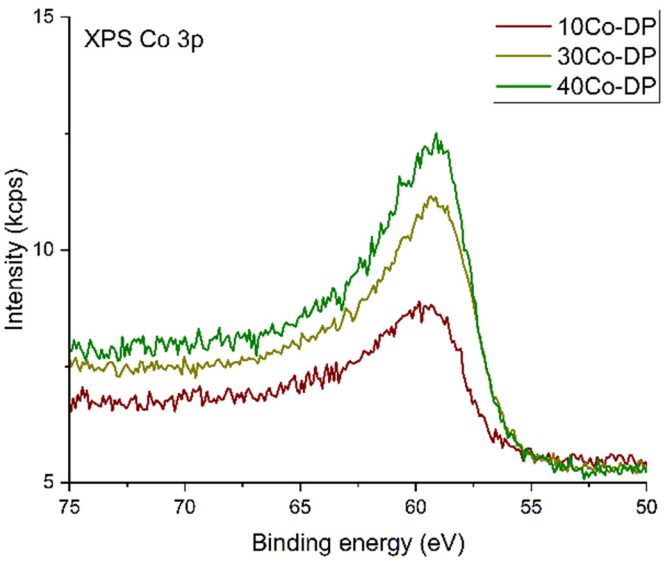

Fig. 7 X-ray photoelectron spectra of Co 3p line of the selected *x*Co-DP (*x* = 10, 30, 40) catalysts.

precursor is reduced to metallic cobalt. This is evidenced by the position of the XPS Co 3p line maximum at 59–60 eV, characteristic of metallic cobalt.[51] For oxidised cobalt species, these lines would be shifted to approximately 61 eV.[52]

HAADF-STEM images and EDX elemental mapping of the main catalyst components (Co, Ba, Ce) are shown in Fig. 8.

For all the catalysts, the EDX maps of Ba overlap with Ce, showing no distinct particles containing separate Ba or Ce phases. For the catalysts with low Co loadings, 10Co-DP and 20Co-DP, the Co nanoparticles were relatively spherical and evenly distributed across the support. With further increasing Co loading, a pronounced agglomeration of Co particles was observed. The Co NPs consisted of dense agglomerates of various shapes, with particle size increasing with Co content and ranging from 50–150 nm for 10Co-DP to 150–500 nm for 50Co-DP. Due to significant Co agglomeration, only for catalysts loaded with 10–30 wt% Co was it possible to calculate a clear particle size distribution (Fig. 8). The thus-

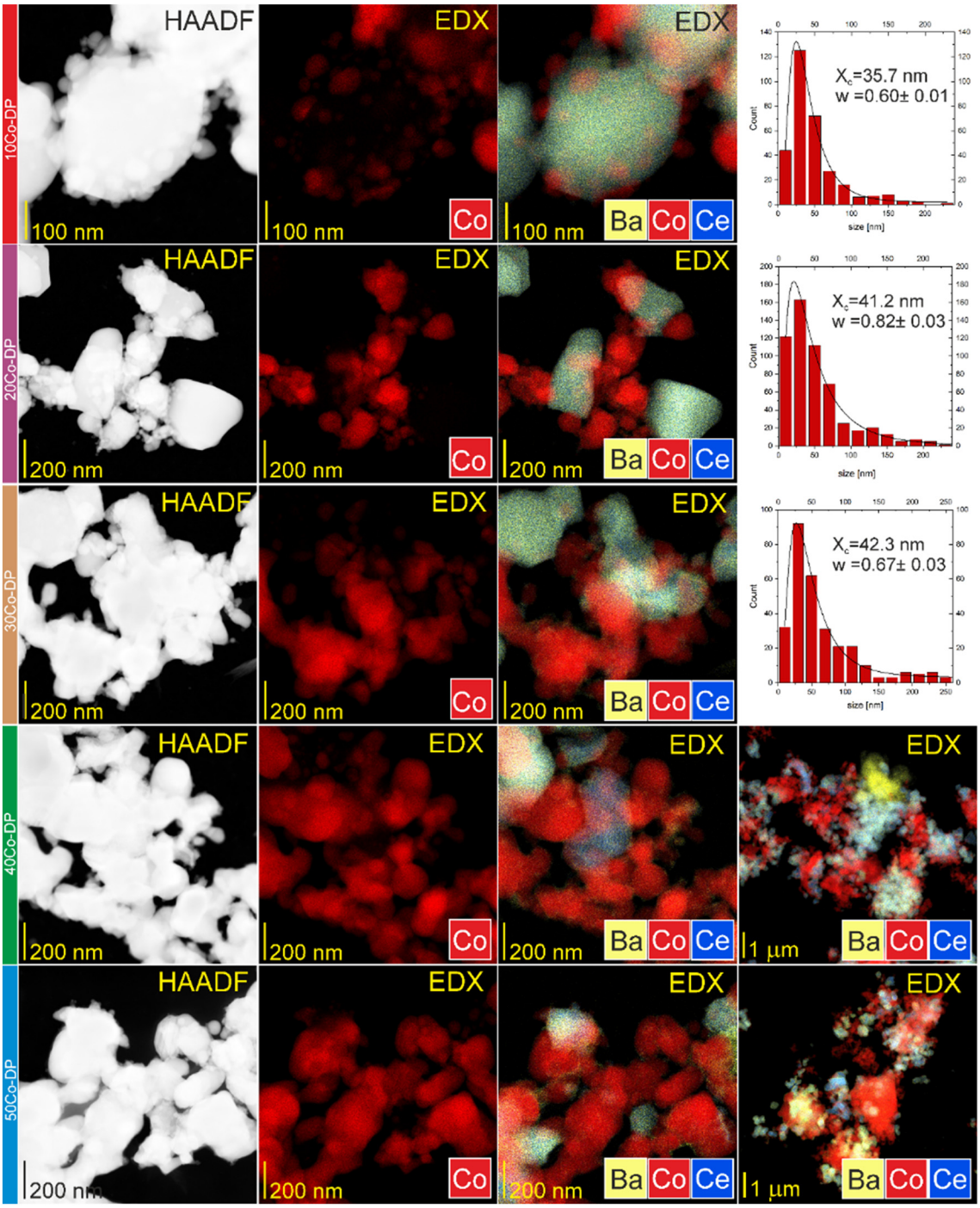

Fig. 8 HAADF-STEM image and corresponding EDX maps of the *x*Co-DP (*x* = 10, 20, 30, 40, and 50) catalysts.

determined average Co particle sizes are also displayed in Table 1.

For the chemisorptive properties, the basic character was first evaluated using CO_2-TPD (Fig. S10). Since CO_2 adsorption on metallic Co particles is rather weak,[53] the CO_2 desorption peaks corresponded mainly to the surface basicity of the support. The resultant profiles revealed desorption peaks at low temperatures (<150 °C), corresponding to weak basic sites, and broader desorption peaks in the 300–600 °C range, corresponding to medium- and strong-basic sites. However, only the 10Co-DP catalyst exhibited a pronounced desorption peak at (300–600 °C). With further increasing Co loading, the medium- and high-temperature desorption features were diminished and eventually disappeared, suggesting that excessive cobalt leads to partial coverage of the support surface and a reduction in the accessible basic sites. However, these sites may still contribute to electron donation to Co, even though they were not accessible to the CO_2 probe molecules.

The interactions between the hydrogen and cobalt were investigated by H_2-TPD. The m/z = 2 signal, attributed to hydrogen, was continuously monitored during the desorption step. The hydrogen TPD profiles were measured for catalysts reduced at 550 and 600 °C to study the evolution of active sites during reductive activation, as well as for spent catalysts to evaluate changes induced under reaction conditions (Fig. 9A, S11, and S12). First, for the catalysts reduced at 550 °C, two distinct desorption peaks were observed in the temperature ranges of 100–200 °C and 400–600 °C, indicating the presence of hydrogen adsorption sites with weak and strong binding strengths to the Co sites, respectively[42,43] (Fig. S11). As the catalyst reduction temperature increased to 600 °C, the hydrogen desorption behaviour changed (Fig. 9A). Still, two desorption peaks were observed in similar temperature ranges; however, the proportion of weak to strong hydrogen-binding sites changed. Generally, the observed effects in surface heterogeneity might be related to differences in the size and structure of the cobalt. Indeed, as reported by Weststrate *et al.*,[54] the hydrogen concentration under reaction conditions may vary significantly for the different cobalt facets. They revealed that hydrogen desorption on fcc-Co(100) occurs at lower temperatures than from hcp-Co(0001), with an estimated desorption barrier of around 70 kJ mol^{-1}. For hcp-Co(0001), the desorption barrier of about 98 kJ mol^{-1} was found. Moreover, depending on the structure, the desorption behaviour varied. For fcc-Co(100), a single desorption peak was observed, whereas for hcp-Co(0001), two desorption peaks were observed.[54] Taken together, these results indicate the strong dependence of the chemisorption properties on the size and structure of Co. For the catalyst reduced at 600 °C, a more diverse surface landscape was observed, as indicated by LT/HT ratios ranging from 0.58 to 1.58, whereas for the catalyst reduced at 550 °C, the LT/HT ratio ranged from 0.53 to 1.06 (Tables S3 and S8). This pleasurably implied changes in the structure of Co sites, thereby altering the chemisorptive properties. As already mentioned, the presence of weak and strong binding sites in a similar proportion can facilitate dissociative hydrogen adsorption and subsequent reaction with nitrogen to form ammonia.[24] Indeed, when comparing catalyst performance after activation at 550 and 600 °C, the latter was favourable, leading to an increase in the ammonia synthesis rate (Table S9). It is also observed that the H_2 desorption increased with increasing Co loading, reached a maximum at 40 wt% Co, and then decreased as the loading increased to 50 wt% Co (Tables S3 and S8, Fig. S13). Compared to the catalyst reduced at 600 °C, the spent samples exhibited a similar H_2 desorption behaviour, featuring adsorption sites in the low- and high-temperature regions (Fig. S12). Although the peaks retained their positions, a decrease in the intensity of the high-temperature peak could be observed. Furthermore, as shown in Fig. S13, the amount of desorbed hydrogen from the spent catalyst was lower than that from the catalyst reduced at 550 and 600 °C, respectively, confirming partial,

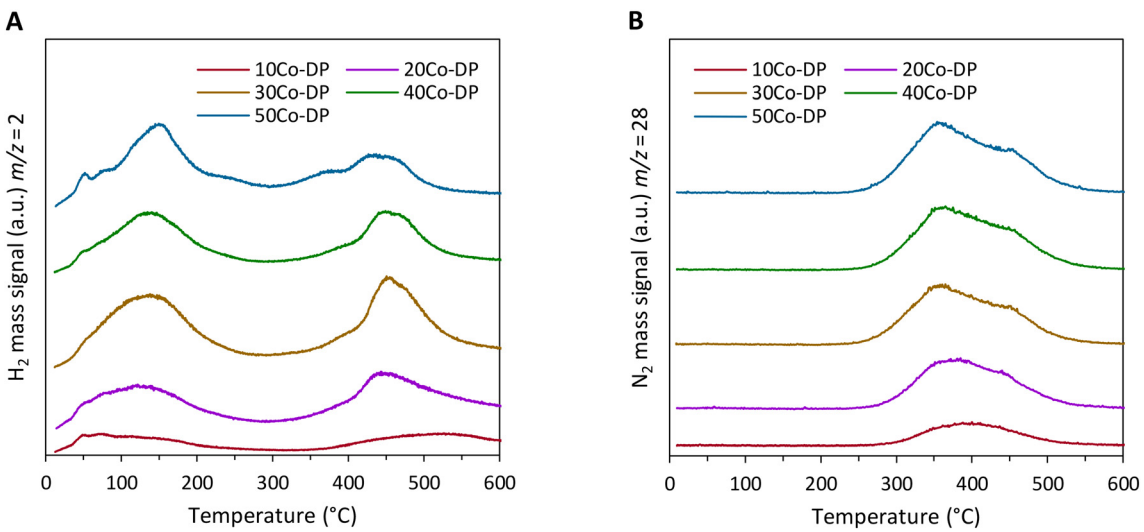

Fig. 9 (A) H_2-TPD and (B) N_2-TPD analyses of the *x*Co-DP (*x* = 10, 20, 30, 40 and 50) catalysts.

but not extensive, sintering. If extensive sintering had occurred, a much more pronounced decrease in H_2 desorption would be expected. Instead, the relatively high H_2 desorption indicates that the Co sites remained greatly present even after prolonged overheating. The results correspond well with the observed stable catalyst performance (Fig. 4D). It also suggests that SMSI can effectively mitigate severe particle agglomeration and preserve catalytic activity over time. Indeed, similar observations were made for Co- and Ru-based catalysts supported on $BaCeO_3$.[23,55] Li *et al.*[55] reported that $Ru/BaCeO_3$ is highly efficient for ammonia synthesis due to the strong electron-donating ability associated with surface basic oxygen species and the presence of oxygen vacancies, which facilitate electron transfer to the active metal and promote N_2 dissociation. Moreover, the formation of strong interfacial bonds (*e.g.*, metal–O–Ce) was shown to enhance electronic metal–support interactions and stabilise the active phase against sintering.

To further evaluate the chemisorptive properties, nitrogen TPD analyses were performed (Fig. 9B). This is important for investigating the interaction between Co and N_2. The m/z = 28 signal, attributed to nitrogen, was continuously monitored during the desorption step. Broad N_2 desorption peaks were observed for the catalysts in the intermediate-to-high temperature region (300–600 °C). The peak shape changed as the Co loading increased. For low loadings, a peak centred around 400 °C was observed, whereas for higher loadings, a desorption feature resulting from two overlapping signals at ~370 and ~450 °C, corresponding to two different adsorption sites, was observed. Generally, the peaks were of low intensity, as is known, because cobalt binds nitrogen weakly.[18,42,56,57] Furthermore, similar to the hydrogen TPD results, the amount of desorbed nitrogen increased with the increasing Co loading, reaching a maximum at 40 wt% Co, and then slightly decreased as the loading increased to 50 wt% Co (Table S10). These indicate that the increase in cobalt loading led to a greater number of nitrogen adsorption sites and differences in N_2 adsorption strength. This suggests that the structure-sensitive nature of nitrogen activation on cobalt surfaces, as reported in,[18,56,57] where N_2 activation strongly depends on size, surface structure, and the coordination of Co.

This heterogeneity in surface adsorption sites for H_2 and N_2 in high cobalt-loading catalysts (≥30 wt% Co) could contribute to their high intrinsic activity (TOF) values, resulting in lower apparent activation energies (Fig. 4). Moreover, the presence of high-temperature desorption features (~400–500 °C) in the H_2-TPD and N_2-TPD profiles suggests that strong adsorption sites may be common to both species (Fig. 9). Although it might imply potential competition between H_2 and N_2 for these sites under reaction conditions, this temperature range coincides with ammonia synthesis conditions, suggesting that these sites are likely catalytically relevant to the reaction. These results also allowed us to conclude that the high hydrogen and nitrogen chemisorption capacities, along with the diverse surface landscapes featuring various adsorption sites, were responsible for the enhanced rate of ammonia synthesis over the high cobalt-loaded catalyst.

These results, together with those for the metal deposition effects (*section 3.1*), highlight the crucial roles of the metal deposition method and metal loading in tailoring the size and distribution of Co NPs. This, in turn, significantly affects the chemisorptive properties of the Co sites, thereby tuning their reactivity. This clearly demonstrates that the ammonia synthesis over Co-based catalysts is a structure-sensitive reaction, and its activity depends on the cobalt structure, which is known to be size-dependent.[35] Any small change in catalyst structure could result in a change in performance. Kitakami *et al.*[37] reported a close relationship between the size and structure of cobalt. They revealed that Co particles of <20 nm size are of fcc structure, 20–30 nm are a mixture of fcc and hcp structures, and >40 nm are of hcp structure. Meanwhile, as revealed by Rambeau *et al.*,[35] the ammonia synthesis reaction occurs on metallic Co at different rates depending on the structure. It was found that the hcp-Co exhibits higher activity (8×10^{-4} s^{-1}) on ammonia formation than the fcc-Co (4×10^{-4} s^{-1}). However, at about 700 K, Co undergoes a phase transition from the hcp to fcc.[36] Although bulk XRD indicates a predominantly fcc-Co phase (Fig. 6), it was revealed that for high cobalt-loaded catalysts, it was likely that the domains of the hcp-Co structure were also present. These may be stabilised to a limited extent even at elevated temperatures due to local defects or surface effects, particularly at steps and kinks, as revealed by Weststrate *et al.*[54] Meanwhile, the specific support or promoter may further stabilise hcp-Co domains in the individual Co NPs. Metal–support interactions or electronic effects induced by promoter addition can stabilise hcp-Co domains at temperatures where bulk Co would normally adopt the fcc structure. Indeed, previous studies on ammonia synthesis catalysed by cobalt nanoparticles (NPs) have shown that it is sensitive to size and structure. Zybert *et al.*[34] studied the Ba-promoted Co/C catalysts in which the Co size varied from 3 to 45 nm. They revealed a correlation between the reactivity of the cobalt surface in ammonia synthesis and cobalt particle size. The dependence of intrinsic activity (TOF) on cobalt particle size indicates that there is an optimal size for cobalt particles (20–30 nm), ensuring the highest activity of the cobalt catalyst in the ammonia synthesis reaction. The observed effect is mainly ascribed to changes in the Co structure. For particles with a diameter of 20–30 nm, except for the fcc-Co phase, the hcp-Co phase also appears, which, along with still a high Co dispersion, leads to the high catalyst activity. Notably, despite the harsh ammonia synthesis reaction conditions, which typically favour the formation of the thermodynamically stable fcc-Co phase, the authors observed the co-existence of the hcp-Co phase for particles with diameters of 20–30 nm, suggesting that an appropriate support and promoter can stabilise the hcp-Co structure under ammonia synthesis conditions. Similar

observations were also made for Co/C catalysts used in Fischer–Tropsch synthesis (FTS). Herold *et al.*[58] revealed that support properties and Co phase composition are likely interconnected, and differences in Co phase composition after reduction likely arise from the properties of support. They found that Co NPs consist of intergrown fcc and hcp domains, even though the Co nanoparticle sizes determined by STEM were about 7.5 nm.[58] This phenomenon of structure sensitivity in ammonia synthesis was also observed for other catalysts, including Fe- and Ru-based ones.[59–62] Jacobsen *et al.*[61] reported that the support type plays a decisive role in controlling the Ru structure and the resulting changes in the abundance of B5-type sites, which are often considered the most active for N_2 activation in ammonia synthesis. These so-called B5 sites consist of a specific geometric arrangement of five Ru atoms, exposing three-fold hollow and bridge sites that strongly facilitate N≡N bond cleavage.[62] The authors demonstrated that differences in support properties influence the morphology and size distribution of Ru, leading to pronounced variations in the availability of B5-type sites even when overall dispersion is similar; this structural sensitivity, rather than simple metal dispersion, was identified as the primary cause of variations in catalytic activity across different supported Ru systems.[61,62]

Taking all these results together, we showed that by modulating the Co loading amounts, different dispersed catalysts with distinct nanoparticle sizes were obtained. This, in turn, affected the Co properties, resulting in an increase in intrinsic activity with increasing Co loading, reaching a maximum at 40 wt% Co, and then slightly decreased. We attribute the superior activity of the catalyst loaded with 40 wt% Co to its highest hydrogen and nitrogen chemisorption capacities, as well as to its most diverse surface landscape, featuring various adsorption sites. This favourable surface heterogeneity is supposedly related to the Co structure and size, which are interconnected, as discussed previously.

4. Conclusions

In the present study, we investigated the effects of the cobalt deposition method and cobalt loadings on the physicochemical properties and catalytic performance in ammonia synthesis. The cobalt catalysts supported on samarium-doped barium cerate were prepared using different deposition methods, that is, deposition–precipitation (DP), wet impregnation (WI), and physical mixing (PM). It has been revealed that, depending on the method used, the catalyst properties vary in terms of chemisorptive properties and catalytic activity. High activity observed for the catalysts obtained by the DP and WI methods is mainly due to the diverse surface landscape, facilitating the hydrogen and nitrogen activation. A series of catalysts with different Co loadings, ranging from 10 to 50 wt%, was then prepared using the DP method. A clear dependence of the catalytic activity on the amount of deposited Co was observed. Specifically, the reaction rate and the intrinsic reaction rate increased with increasing Co loading, reached a maximum at 40 wt% Co, and then slightly decreased. The favourable catalytic properties of high cobalt-loading catalysts (≥30 wt% Co) are mainly attributed to the structural sensitivity of ammonia synthesis over Co sites rather than to dispersion effects. The catalyst loaded with 40 wt% Co was particularly active, exhibiting the highest hydrogen chemisorption capacity and the most diverse surface landscape, featuring various adsorption sites. The findings also underscore the superior performance of the developed catalysts, as revealed by comparison with industrial iron ammonia synthesis catalysts, highlighting the prospects for further development.

Author contributions

Hubert Ronduda: conceptualisation, methodology, investigation, writing – original draft, writing – review & editing, visualisation, supervision. Małgorzata Lemańska: investigation. Urszula Ulkowska: investigation. Wojciech Patkowski: investigation. Weronika Bulejak: investigation. Jacek Sikorski: investigation. Andrzej Ostrowski: investigation. Kamil Sobczak: investigation, visualisation. Milena Ojrzyńska: investigation, visualisation. Dariusz Moszyński: investigation, writing – original draft, visualisation. Wioletta Raróg-Pilecka: investigation, funding acquisition.

Conflicts of interest

The authors declare that they have no known competing financial interests or personal relationships that could have appeared to influence the work reported in this paper.

Data availability

The data supporting this article have been included as part of the supplementary information (SI).

Supplementary information is available. See DOI: https://doi.org/10.1039/d5cy01610j.

Acknowledgements

Research was funded by Warsaw University of Technology within the Excellence Initiative: Research University (IDUB) programme. Hubert Ronduda acknowledges the support from the Foundation for Polish Science within the START 2025 program. We also thank Dr Magdalena Zybert for valuable feedback on the manuscript.

References

1 J. Humphreys, R. Lan and S. Tao, Development and Recent Progress on Ammonia Synthesis Catalysts for Haber–Bosch Process, *Adv. Energy Sustainability Res.*, 2021, **2**, 2000043, DOI: 10.1002/aesr.202000043.

2 L. Torrente-Murciano and C. Smith, Process challenges of green ammonia production, *Nat. Synth.*, 2023, **2**, 587–588, DOI: 10.1038/s44160-023-00339-x.

3 R. W. Howarth and M. Z. Jacobson, How green is blue hydrogen?, *Energy Sci. Eng.*, 2021, **9**, 1676–1687, DOI: 10.1002/ese3.956.
4 D. Ye and S. C. E. Tsang, Prospects and challenges of green ammonia synthesis, *Nat. Synth.*, 2023, **2**, 612–623, DOI: 10.1038/s44160-023-00321-7.
5 B. Lee, L. R. Winter, H. Lee, D. Lim, H. Lim and M. Elimelech, Pathways to a green ammonia future, *ACS Energy Lett.*, 2022, **7**, 3032–3038, DOI: 10.1021/acsenergylett.2c01615.
6 K. H. R. Rouwenhorst, Y. Engelmann, K. van't Veer, R. S. Postma, A. Bogaerts and L. Lefferts, Plasma-driven catalysis: green ammonia synthesis with intermittent electricity, *Green Chem.*, 2020, **22**, 6258–6287, DOI: 10.1039/D0GC02058C.
7 P. Mehta, P. M. Barboun, Y. Engelmann, D. B. Go, A. Bogaerts, W. F. Schneider and J. C. Hicks, Plasma-Catalytic Ammonia Synthesis beyond the Equilibrium Limit, *ACS Catal.*, 2020, **10**, 6726–6734, DOI: 10.1021/acscatal.0c00684.
8 A. Sousa, D. Mateo, L. Garzon-Tovar, K. Brennan, A. Rendón-Patiño, N. Morlanés, X. Wang, J. C. Navarro, J. Ruiz-Martinez, M. García-Melchor and J. Gascon, Unlocking Low-Temperature Ammonia Decomposition via an Iron Metal–Organic Framework-Derived Catalyst Under Photo-Thermal Conditions, *Small*, 2025, **21**, 2411468, DOI: 10.1002/smll.202411468.
9 C. Li, Y. Shi, Z. Zhang, J. Ni, X. Wang, J. Lin, B. Lin and L. Jiang, Improving the ammonia synthesis activity of Ru/CeO_2 through enhancement of the metal–support interaction, *J. Energy Chem.*, 2021, **60**, 403–409, DOI: 10.1016/j.jechem.2021.01.031.
10 W. Li, S. Wang and J. Li, Effect of rare earth elements (La, Y, Pr) in multi-element composite perovskite oxide supports for ammonia synthesis, *J. Rare Earths*, 2021, **39**, 427–433, DOI: 10.1016/j.jre.2020.06.006.
11 Z. Wang, B. Liu and J. Liu, Highly effective perovskite-type $BaZrO_3$ supported Ru catalyst for ammonia synthesis, *Appl. Catal., A*, 2013, **458**, 130–136, DOI: 10.1016/j.apcata.2013.03.037.
12 J. Ni, S. Shi, C. Zhang, B. Fang, X. Wang, J. Lin, S. Liang, B. Lin and L. Jiang, Enhanced catalytic performance of the carbon-supported Ru ammonia synthesis catalyst by an introduction of oxygen functional groups via gas-phase oxidation, *J. Catal.*, 2022, **409**, 78–86, DOI: 10.1016/j.jcat.2022.03.026.
13 B. Lin, Y. Guo, C. Cao, J. Ni, J. Lin and L. Jiang, Carbon support surface effects in the catalytic performance of Ba-promoted Ru catalyst for ammonia synthesis, *Catal. Today*, 2018, **316**, 230–236, DOI: 10.1016/j.cattod.2018.01.008.
14 K. Lee, R. Woo, H. C. Woo, G. Ko, K. Cho, Y. Park, M. Choi and H. C. Yoon, Unraveling the role of MgO in the Ru-Ba/MgO catalyst for boosting ammonia synthesis: Comparative study of MgO and $MgAlO_x$ supports, *J. Catal.*, 2024, **434**, 115530, DOI: 10.1016/j.jcat.2024.115530.
15 R. Li, L. Liu, X. Ju, J. Feng, J. Wang, J. Guo, T. He and P. Chen, Interaction Between Ru Nanoparticles and Pr_6O_{11} Triggers Catalytic Ammonia Synthesis, *Catal. Lett.*, 2024, **154**, 4814–4822, DOI: 10.1007/s10562-024-04629-7.
16 R. J. Kaleńczuk, Effect of cobalt on the morphology and activity of fused iron catalyst for ammonia synthesis, *Appl. Catal., A*, 1994, **112**, 149–160, DOI: 10.1016/0926-860X(94)80216-5.
17 S. Hagen, R. Barford, R. Fehrmann, C. J. H. Jacobsen, H. T. Teunissen and I. Chorkendorff, Ammonia synthesis with barium-promoted iron–cobalt alloys supported on carbon, *J. Catal.*, 2003, **214**, 327–335, DOI: 10.1016/S0021-9517(02)00182-3.
18 B.-Y. Zhang, P.-P. Chen, J.-X. Liu, H.-Y. Su and W.-X. Li, Influence of Cobalt Crystal Structures on Activation of Nitrogen Molecule: A First-Principles Study, *J. Phys. Chem. C*, 2019, **123**, 10956–10966, DOI: 10.1021/acs.jpcc.9b00590.
19 B. Lin, Y. Liu, L. Heng, J. Ni, J. Ni, J. Lin and L. Jiang, Effect of barium and potassium promoter on Co/CeO_2 catalysts in ammonia synthesis, *J. Rare Earths*, 2018, **36**, 703–707, DOI: 10.1016/j.jre.2018.01.017.
20 B. Lin, Y. Qi, K. Wei and J. Lin, Effect of pretreatment on ceria-supported cobalt catalyst for ammonia synthesis, *RSC Adv.*, 2014, **4**, 38093–38102, DOI: 10.1039/C4RA06175F.
21 M. Karolewska, E. Truszkiewicz, M. Wściseł, B. Mierzwa, L. Kępiński and W. Raróg-Pilecka, Ammonia synthesis over a Ba and Ce-promoted carbon-supported cobalt catalyst. Effect of the cerium addition and preparation procedure, *J. Catal.*, 2013, **303**, 130–134, DOI: 10.1016/j.jcat.2013.03.005.
22 H. Ronduda, M. Lemańska, U. Ulkowska, W. Patkowski, A. Ostrowski, K. Sobczak and W. Raróg-Pilecka, Enhanced ammonia synthesis over barium cerate-supported cobalt catalyst by rare-earth element doping, *Catal. Today*, 2025, **456**, 115342, DOI: 10.1016/j.cattod.2025.115342.
23 M. Zybert, H. Ronduda, W. Patkowski, A. Ostrowski, K. Sobczak and W. Raróg-Pilecka, Improving the catalytic performance of Co/$BaCeO_3$ catalyst for ammonia synthesis by Y-modification of the perovskite-type support, *RSC Adv.*, 2024, **14**, 36281–36294, DOI: 10.1039/D4RA06251E.
24 H. Ronduda, M. Zybert, W. Patkowski, A. Tarka, P. Jodłowski, L. Kępiński, A. Sarnecki, D. Moszyński and W. Raróg-Pilecka, Tuning the catalytic performance of Co/Mg-La system for ammonia synthesis via the active phase precursor introduction method, *Appl. Catal., A*, 2020, **598**, 117553, DOI: 10.1016/j.apcata.2020.117553.
25 K. Sato, S. Miyahara, K. Tsujimaru, Y. Wada, T. Toriyama, T. Yamamoto, S. Matsumura, K. Inazu, H. Mohri, T. Iwasa, T. Taketsugu and K. Nagaoka, Barium Oxide Encapsulating Cobalt Nanoparticles Supported on Magnesium Oxide: Active Non-Noble Metal Catalysts for Ammonia Synthesis under Mild Reaction Conditions, *ACS Catal.*, 2021, **11**, 13050–13061, DOI: 10.1021/acscatal.1c02887.
26 A. Sfeir, C. A. Teles, C. Ciotonea, G. N. Manjunatha Reddy, M. Marinova, J. Dhainaut, A. Löfberg, J.-P. Dacquin, S. Royer and S. Laassiri, Enhancing ammonia catalytic production over spatially confined cobalt molybdenum nitride nanoparticles in SBA-15, *Appl. Catal., B*, 2023, **325**, 122319, DOI: 10.1016/j.apcatb.2022.122319.

27 G. Zhong, Y. Liu, S. Yu, C. Zhang, J. Ni, J. Lin, B. Lin and L. Jiang, Strengthening Hydrogen Spillover in Ceria-Supported Co–Fe Bimetallic Catalysts for Boosting Ammonia Synthesis, *Ind. Eng. Chem. Res.*, 2024, **63**, 5089–5096, DOI: 10.1021/acs.iecr.3c04299.

28 R. K. Rai, R. Maligal-Ganesh, W. Al Maksoud, S.-J. Kim, Y. Vaishnav, C. T. Yavuz and Y. Kobayashi, Enhancing Ammonia Synthesis on Co_3Mo_3N via Metal Support Interactions on a Single-crystalline MgO Support, *ChemCatChem*, 2024, **16**, e202301579, DOI: 10.1002/cctc.202301579.

29 P. Munnik, P. E. de Jongh and K. P. de Jong, Recent Developments in the Synthesis of Supported Catalysts, *Chem. Rev.*, 2015, **115**, 6687–6718, DOI: 10.1021/cr500486u.

30 J. Ruiz-Martínez, A. Sepúlveda-Escribano, J. A. Anderson and F. Rodríguez-Reinoso, Influence of the preparation method on the catalytic behaviour of $PtSn/TiO_2$ catalysts, *Catal. Today*, 2007, **123**, 235–244, DOI: 10.1016/j.cattod.2007.02.01.

31 E. Marceau, X. Carrier, M. Che, O. Clause and C. Marcilly, Ion Exchange and Impregnation, in *Handbook of Heterogeneous Catalysis*, ed. G. Ertl, H. Knözinger, F. Schüth and J. Weitkamp, 2008, DOI: 10.1002/9783527610044.hetcat0022.

32 J. W. Geus and A. J. Dillen, Preparation of Supported Catalysts by Deposition–Precipitation, in *Handbook of Heterogeneous Catalysis*, ed. G. Ertl, H. Knözinger, F. Schüth and J. Weitkamp, 2008, DOI: 10.1002/9783527610044.hetcat0021.

33 H. Ronduda, M. Zybert, W. Patkowski, K. Sobczak, D. Moszyński, A. Albrecht, A. Sarnecki and W. Raróg-Pilecka, On the effect of metal loading on the performance of Co catalysts supported on mixed $MgO–La_2O_3$ oxides for ammonia synthesis, *RSC Adv.*, 2022, **12**, 33876–33888, DOI: 10.1039/D2RA06053A.

34 M. Zybert, A. Tarka, W. Patkowski, H. Ronduda, B. Mierzwa, L. Kępiński and W. Raróg-Pilecka, Structure Sensitivity of Ammonia Synthesis on Cobalt: Effect of the Cobalt Particle Size on the Activity of Promoted Cobalt Catalysts Supported on Carbon, *Catalysts*, 2022, **12**, 1285, DOI: 10.3390/catal12101285.

35 G. Rambeau, A. Jorti and H. Amariglio, Catalytic activity of a cobalt powder in NH3 synthesis in relation with the allotropic transformation of the metal, *J. Catal.*, 1985, **94**, 155–165, DOI: 10.1016/0021-9517(85)90091-0.

36 R. Lizárraga, F. Pan, L. Bergqvist, E. Holmström, Z. Gercsi and L. Vitos, First Principles Theory of the hcp-fcc Phase Transition in Cobalt, *Sci. Rep.*, 2017, **7**, 3778, DOI: 10.1038/s41598-017-03877-5.

37 O. Kitakami, H. Sato, Y. Shimada, F. Sato and M. Tanaka, Size effect on the crystal phase of cobalt fine particles, *Phys. Rev. B: Condens. Matter Mater. Phys.*, 1997, **56**, 13849–13854, DOI: 10.1103/PhysRevB.56.13849.

38 J.-I. Jung and D. D. Edwards, X-ray photoelectron (XPS) and Diffuse Reflectance Infra Fourier Transformation (DRIFT) study of $Ba_{0.5}Sr_{0.5}Co_xFe_{1-x}O_{3-\delta}$ (BSCF: x=0–0.8) ceramics, *J. Solid State Chem.*, 2011, **184**, 2238–2243, DOI: 10.1016/j.jssc.2011.06.016.

39 Z. Kowalczyk, Effect of potassium on the high pressure kinetics of ammonia synthesis over fused iron catalyst, *Catal. Lett.*, 1996, **37**, 173–179, DOI: 10.1007/BF00807750.

40 Z. Kowalczyk, J. Sentek, S. Jodzis, M. Muhler and O. Hinrichsen, Effect of Potassium on the Kinetics of Ammonia Synthesis and Decomposition over Fused Iron Catalyst at Atmospheric Pressure, *J. Catal.*, 1997, **169**, 407–414, DOI: 10.1006/jcat.1997.1664.

41 R. C. Reuel and C. H. Bartholomew, The stoichiometries of H_2 and CO adsorptions on cobalt: Effect of support and preparation, *J. Catal.*, 1984, **85**, 63–77, DOI: 10.1016/0021-9517(84)90110-6.

42 X. Wang, L. Li, T. Zhang, B. Lin, J. Ni, C.-T. Au and L. Jiang, Strong metal–support interactions of Co-based catalysts facilitated by dopamine for highly efficient ammonia synthesis: in situ XPS and XAFS spectroscopy coupled with TPD studies, *Chem. Commun.*, 2019, **55**, 474–477, DOI: 10.1039/C8CC07130F.

43 C. Li, S. Yu, Y. Shi, M. Li, B. Fang, J. Lin, J. Ni, X. Wang, B. Lin and L. Jiang, Combining silica to boost the ammonia synthesis activity of ceria-supported Ru catalyst, *Chem. Eng. Sci.*, 2022, **262**, 118045, DOI: 10.1016/j.ces.2022.118045.

44 C. J. Weststrate, M. Mahmoodinia, M. H. Farstad, I.-H. Svenum, M. D. Strømsheim, J. W. Niemantsverdriet and H. J. Venvik, Interaction of hydrogen with flat (0001) and corrugated (11–20) and (10–12) cobalt surfaces: Insights from experiment and theory, *Catal. Today*, 2020, **342**, 124–130, DOI: 10.1016/j.cattod.2019.04.002.

45 W. Patkowski, M. Zybert, H. Ronduda, G. Gawrońska, A. Albrecht, D. Moszyński, A. Fidler, P. Dłużewski and W. Raróg-Pilecka, The Influence of Active Phase Content on Properties and Activity of Nd_2O_3-Supported Cobalt Catalysts for Ammonia Synthesis, *Catalysts*, 2023, **13**, 405, DOI: 10.3390/catal13020405.

46 B. Tomić-Tucaković, D. Majstorović, D. Jelić and S. Mentus, Thermogravimetric study of the kinetics of Co_3O_4 reduction by hydrogen, *Thermochim. Acta*, 2012, **541**, 15–24, DOI: 10.1016/j.tca.2012.04.018.

47 O. A. Kungurova, N. V. Shtertser, E. G. Koemets, S. V. Cherepanova and A. A. Khassin, The effect of ruthenium promotion of the $Co/\delta\text{-}Al_2O_3$ catalyst on the hydrogen reduction kinetics of cobalt, *React. Kinet., Mech. Catal.*, 2017, **120**, 501–525, DOI: 10.1007/s11144-016-1118-2.

48 D. Potoczna-Petru and L. Kępiński, Reduction study of Co_3O_4 model catalyst by electron microscopy, *Catal. Lett.*, 2001, **73**, 41–46, DOI: 10.1023/A:1009022202448.

49 L. Ilieva, P. Petrova, A. M. Venezia, E. M. Anghel, R. State, G. Avdeev and T. Tabakova, Mechanochemically Prepared Co_3O_4-CeO_2 Catalysts for Complete Benzene Oxidation, *Catalysts*, 2021, **11**, 1316, DOI: 10.3390/catal11111316.

50 S. Asal, M. Saif, H. Hafez, S. Mozia, A. Heciak, D. Moszyński and M. S. A. Abdel-Mottaleb, Photocatalytic generation of useful hydrocarbons and hydrogen from acetic acid in the presence of lanthanide modified TiO_2, *Int. J. Hydrogen Energy*, 2011, **36**, 6529–6537, DOI: 10.1016/j.ijhydene.2011.02.066.

51 A. Sarnecki, P. Adamski, A. Albrecht, A. Komorowska, M. Nadziejko and D. Moszyński, XPS study of cobalt-ceria catalysts for ammonia synthesis – The reduction process, *Vacuum*, 2018, **155**, 434–438, DOI: 10.1016/j.vacuum.2018.06.034.

52 L. Dahéron, R. Dedryvère, H. Martinez, M. Ménétrier, C. Denage, C. Delmas and D. Gonbeau, Electron Transfer Mechanisms upon Lithium Deintercalation from $LiCoO_2$ to CoO_2 Investigated by XPS, *Chem. Mater.*, 2008, **20**, 583–590, DOI: 10.1021/cm702546s.

53 C. G. Visconti, L. Lietti, E. Tronconi, P. Forzatti, R. Zennaro and E. Finocchio, Fischer–Tropsch synthesis on a Co/Al_2O_3 catalyst with CO_2 containing syngas, *Appl. Catal., A*, 2009, **355**, 61–69, DOI: 10.1016/j.apcata.2008.11.027.

54 C. J. Weststrate, D. G. Rodriguez, D. Sharma and J. W. Niemantsverdriet, Structure-dependent adsorption and desorption of hydrogen on FCC and HCP cobalt surfaces, *J. Catal.*, 2022, **405**, 303–312, DOI: 10.1016/j.jcat.2021.12.016.

55 W. Li, S. Wang and J. Li, Highly Effective $Ru/BaCeO_3$ Catalysts on Supports with Strong Basic Sites for Ammonia Synthesis, *Chem. – Asian J.*, 2019, **14**, 2815–2821, DOI: 10.1002/asia.201900618.

56 C. J. H. Jacobsen, S. Dahl, B. S. Clausen, S. Bahn, A. Logadottir and J. K. Nørskov, Catalyst design by interpolation in the periodic table: bimetallic ammonia synthesis catalysts, *J. Am. Chem. Soc.*, 2001, **123**, 8404–8405, DOI: 10.1021/ja010963d.

57 Y. Tsuji, K. Ogasawara, M. Kitano, K. Kishida, H. Abe, Y. Niwa, T. Yokoyama, M. Hara and H. Hosono, Control of nitrogen activation ability by Co-Mo bimetallic nanoparticle catalysts prepared *via* sodium naphthalenide-reduction, *J. Catal.*, 2018, **364**, 31–39, DOI: 10.1016/j.jcat.2018.04.029.

58 F. Herold, D. de Oliveira, G. Baade, J. Friedland, R. Güttel, M. Claeys and M. Rønning, Is Carbon Heteroatom Doping the Key to Active and Stable Carbon Supported Cobalt Fischer–Tropsch Catalysts?, *ACS Catal.*, 2025, **15**, 6673–6689, DOI: 10.1021/acscatal.4c08092.

59 N. D. Spencer, R. C. Schoonmaker and G. A. Somorjai, Iron single crystals as ammonia synthesis catalysts: Effect of surface structure on catalyst activity, *J. Catal.*, 1982, **74**, 129–135, DOI: 10.1016/0021-9517(82)90016-1.

60 G. A. Somorjai and N. Materer, Surface structures in ammonia synthesis, *Top. Catal.*, 1994, **1**, 215–231, DOI: 10.1007/BF01492277.

61 C. J. H. Jacobsen, S. Dahl, P. L. Hansen, E. Törnqvist, L. Jensen, H. Topsøe, D. V. Prip, P. B. Møenshaug and I. Chorkendorff, Structure sensitivity of supported ruthenium catalysts for ammonia synthesis, *J. Mol. Catal. A: Chem.*, 2000, **163**, 19–26, DOI: 10.1016/S1381-1169(00)00396-4.

62 S. Dahl, A. Logadottir, R. C. Egeberg, J. H. Larsen, I. Chorkendorff, E. Törnqvist and J. K. Nørskov, Role of Steps in N_2 Activation on Ru(0001), *Phys. Rev. Lett.*, 1999, **83**, 1814–1817, DOI: 10.1103/PhysRevLett.83.1814.

